

Dijet Production in Charged and Neutral Current e^+p Interactions at High Q^2

H1 Collaboration

Abstract

Jet production in charged and neutral current events in the kinematic range of Q^2 from 640 to 35 000 GeV^2 is studied in deep-inelastic positron-proton scattering at HERA. The measured rate of multi-jet events and distributions of jet polar angle, transverse energy, dijet mass, and other dijet variables are presented. Using parton densities derived from inclusive DIS cross sections, perturbative QCD calculations in NLO are found to give a consistent description of both the neutral and charged current dijet production. A direct, model independent comparison of the jet distributions in charged and neutral current events confirms that the QCD dynamics of the hadronic final state is independent of the underlying electroweak scattering process.

submitted to Eur. Phys. J. C

C. Adloff³³, V. Andreev²⁴, B. Andrieu²⁷, V. Arkadov³⁵, A. Astvatsatourov³⁵, I. Ayyaz²⁸,
 A. Babaev²³, J. Bähr³⁵, P. Baranov²⁴, E. Barrelet²⁸, W. Bartel¹⁰, U. Bassler²⁸, P. Bate²¹,
 A. Beglarian³⁴, O. Behnke¹⁰, C. Beier¹⁴, A. Belousov²⁴, T. Benisch¹⁰, Ch. Berger¹,
 G. Bernardi²⁸, T. Berndt¹⁴, J.C. Bizot²⁶, K. Borrás⁷, V. Boudry²⁷, W. Braunschweig¹,
 V. Brisson²⁶, H.-B. Bröker², D.P. Brown²¹, W. Brückner¹², P. Bruel²⁷, D. Bruncko¹⁶,
 J. Bürger¹⁰, F.W. Büsler¹¹, A. Bunyatyan^{12,34}, H. Burkhardt¹⁴, A. Burrage¹⁸, G. Buschhorn²⁵,
 A.J. Campbell¹⁰, J. Cao²⁶, T. Carli²⁵, S. Caron¹, E. Chabert²², D. Clarke⁵, B. Clerbaux⁴,
 C. Collard⁴, J.G. Contreras^{7,41}, J.A. Coughlan⁵, M.-C. Cousinou²², B.E. Cox²¹, G. Cozzika⁹,
 J. Cvach²⁹, J.B. Dainton¹⁸, W.D. Dau¹⁵, K. Daum^{33,39}, M. David^{9,†}, M. Davidsson²⁰,
 B. Delcourt²⁶, N. Delerue²², R. Demirchyan³⁴, A. De Roeck^{10,43}, E.A. De Wolf⁴,
 C. Diaconu²², P. Dixon¹⁹, V. Dodonov¹², J.D. Dowell³, A. Droutskoi²³, C. Duprel²,
 G. Eckerlin¹⁰, D. Eckstein³⁵, V. Efremenko²³, S. Egli³², R. Eichler³⁶, F. Eisele¹³,
 E. Eisenhandler¹⁹, M. Ellerbrock¹³, E. Elsen¹⁰, M. Erdmann^{10,40,e}, W. Erdmann³⁶,
 P.J.W. Faulkner³, L. Favart⁴, A. Fedotov²³, R. Felst¹⁰, J. Ferencei¹⁰, S. Ferron²⁷,
 M. Fleischer¹⁰, G. Flügge², A. Fomenko²⁴, I. Foresti³⁷, J. Formánek³⁰, J.M. Foster²¹,
 G. Franke¹⁰, E. Gabathuler¹⁸, K. Gabathuler³², J. Garvey³, J. Gassner³², J. Gayler¹⁰,
 R. Gerhards¹⁰, S. Ghazaryan³⁴, L. Goerlich⁶, N. Gogitidze²⁴, M. Goldberg²⁸, C. Goodwin³,
 C. Grab³⁶, H. Grässler², T. Greenshaw¹⁸, G. Grindhammer²⁵, T. Hadig¹, D. Haidt¹⁰,
 L. Hajduk⁶, W.J. Haynes⁵, B. Heinemann¹⁸, G. Heinzelmann¹¹, R.C.W. Henderson¹⁷,
 S. Hengstmann³⁷, H. Henschel³⁵, R. Heremans⁴, G. Herrera^{7,41}, I. Herynek²⁹, M. Hilgers³⁶,
 K.H. Hiller³⁵, J. Hladký²⁹, P. Höting², D. Hoffmann¹⁰, W. Hoprich¹², R. Horisberger³²,
 S. Hurling¹⁰, M. Ibbotson²¹, Ç. İşsever⁷, M. Jacquet²⁶, M. Jaffre²⁶, L. Janauschek²⁵,
 D.M. Jansen¹², X. Janssen⁴, V. Jemanov¹¹, L. Jönsson²⁰, D.P. Johnson⁴, M.A.S. Jones¹⁸,
 H. Jung²⁰, H.K. Kästli³⁶, D. Kant¹⁹, M. Kapichine⁸, M. Karlsson²⁰, O. Karschnick¹¹,
 O. Kaufmann¹³, M. Kausch¹⁰, F. Keil¹⁴, N. Keller³⁷, J. Kennedy¹⁸, I.R. Kenyon³,
 S. Kermiche²², C. Kiesling²⁵, M. Klein³⁵, C. Kleinwort¹⁰, G. Knies¹⁰, B. Koblitz²⁵,
 S.D. Kolya²¹, V. Korbel¹⁰, P. Kostka³⁵, S.K. Kotelnikov²⁴, M.W. Krasny²⁸, H. Krehbiel¹⁰,
 J. Kroseberg³⁷, D. Krücker³⁸, K. Krüger¹⁰, A. Küpper³³, T. Kuhr¹¹, T. Kurča^{35,16}, R. Kutuev¹²,
 W. Lachnit¹⁰, R. Lahmann¹⁰, D. Lamb³, M.P.J. Landon¹⁹, W. Lange³⁵, T. Laštovička³⁰,
 A. Lebedev²⁴, B. Leißner¹, R. Lemrani¹⁰, V. Lendermann⁷, S. Levonian¹⁰, M. Lindstroem²⁰,
 B. List³⁶, E. Lobodzinska^{10,6}, B. Lobodzinski^{6,10}, N. Laktionova²⁴, V. Lubimov²³, S. Lüders³⁶,
 D. Lüke^{7,10}, L. Lytkin¹², N. Magnussen³³, H. Mahlke-Krüger¹⁰, N. Malden²¹, E. Malinovski²⁴,
 I. Malinovski²⁴, R. Maraček²⁵, P. Marage⁴, J. Marks¹³, R. Marshall²¹, H.-U. Martyn¹,
 J. Martyniak⁶, S.J. Maxfield¹⁸, A. Mehta¹⁸, K. Meier¹⁴, P. Merkel¹⁰, F. Metlica¹², H. Meyer³³,
 J. Meyer¹⁰, P.-O. Meyer², S. Mikocki⁶, D. Milstead¹⁸, T. Mkrtchyan³⁴, R. Mohr²⁵,
 S. Mohrdieck¹¹, M.N. Mondragon⁷, F. Moreau²⁷, A. Morozov⁸, J.V. Morris⁵, K. Müller¹³,
 P. Murín^{16,42}, V. Nagovizin²³, B. Naroska¹¹, J. Naumann⁷, Th. Naumann³⁵, G. Nellen²⁵,
 P.R. Newman³, T.C. Nicholls⁵, F. Niebergall¹¹, C. Niebuhr¹⁰, O. Nix¹⁴, G. Nowak⁶,
 T. Nunnemann¹², J.E. Olsson¹⁰, D. Ozerov²³, V. Panassik⁸, C. Pascaud²⁶, G.D. Patel¹⁸,
 E. Perez⁹, J.P. Phillips¹⁸, D. Pitzl¹⁰, R. Pöschl⁷, I. Potachnikova¹², B. Povh¹², K. Rabbertz¹,
 G. Rädcl⁹, J. Rauschenberger¹¹, P. Reimer²⁹, B. Reisert²⁵, D. Reyna¹⁰, S. Riess¹¹, E. Rizvi³,
 P. Robmann³⁷, R. Roosen⁴, A. Rostovtsev²³, C. Royon⁹, S. Rusakov²⁴, K. Rybicki⁶,
 D.P.C. Sankey⁵, J. Scheins¹, F.-P. Schilling¹³, P. Schlexer¹³, D. Schmidt³³, D. Schmidt¹⁰,
 L. Schoeffel⁹, A. Schöning³⁶, T. Schörner²⁵, V. Schröder¹⁰, H.-C. Schultz-Coulon¹⁰,
 K. Sedlák²⁹, F. Sefkow³⁷, V. Shekelyan²⁵, I. Sheviakov²⁴, L.N. Shtarkov²⁴, G. Siegmon¹⁵,
 P. Sievers¹³, Y. Sirois²⁷, T. Sloan¹⁷, P. Smirnov²⁴, V. Solochenko^{23,†}, Y. Soloviev²⁴,

V. Spaskov⁸, A. Specka²⁷, H. Spitzer¹¹, R. Stamen⁷, J. Steinhart¹¹, B. Stella³¹,
A. Stellberger¹⁴, J. Stiewe¹⁴, U. Straumann³⁷, W. Struczinski², M. Swart¹⁴, M. Taševský²⁹,
V. Tchernyshov²³, S. Tchetchelnitski²³, G. Thompson¹⁹, P.D. Thompson³, N. Tobien¹⁰,
D. Traynor¹⁹, P. Truöl³⁷, G. Tsipolitis³⁶, J. Turnau⁶, J.E. Turney¹⁹, E. Tzamariudaki²⁵,
S. Udluft²⁵, A. Usik²⁴, S. Valkár³⁰, A. Valkárová³⁰, C. Vallée²², P. Van Mechelen⁴,
Y. Vazdik²⁴, S. von Dombrowski³⁷, K. Wacker⁷, R. Wallny³⁷, T. Walter³⁷, B. Waugh²¹,
G. Weber¹¹, M. Weber¹⁴, D. Wegener⁷, A. Wegner²⁵, T. Wengler¹³, M. Werner¹³, G. White¹⁷,
S. Wiesand³³, T. Wilksen¹⁰, M. Winde³⁵, G.-G. Winter¹⁰, C. Wissing⁷, M. Wobisch²,
H. Wollatz¹⁰, E. Wünsch¹⁰, A.C. Wyatt²¹, J. Žáček³⁰, J. Zálešák³⁰, Z. Zhang²⁶, A. Zhokin²³,
F. Zomer²⁶, J. Zsembery⁹ and M. zur Nedden¹⁰

¹ I. Physikalisches Institut der RWTH, Aachen, Germany^a

² III. Physikalisches Institut der RWTH, Aachen, Germany^a

³ School of Physics and Space Research, University of Birmingham, Birmingham, UK^b

⁴ Inter-University Institute for High Energies ULB-VUB, Brussels; Universitaire Instelling Antwerpen, Wilrijk; Belgium^c

⁵ Rutherford Appleton Laboratory, Chilton, Didcot, UK^b

⁶ Institute for Nuclear Physics, Cracow, Poland^d

⁷ Institut für Physik, Universität Dortmund, Dortmund, Germany^a

⁸ Joint Institute for Nuclear Research, Dubna, Russia

⁹ DSM/DAPNIA, CEA/Saclay, Gif-sur-Yvette, France

¹⁰ DESY, Hamburg, Germany^a

¹¹ II. Institut für Experimentalphysik, Universität Hamburg, Hamburg, Germany^a

¹² Max-Planck-Institut für Kernphysik, Heidelberg, Germany^a

¹³ Physikalisches Institut, Universität Heidelberg, Heidelberg, Germany^a

¹⁴ Kirchhoff-Institut für Physik, Universität Heidelberg, Heidelberg, Germany^a

¹⁵ Institut für experimentelle und angewandte Physik, Universität Kiel, Kiel, Germany^a

¹⁶ Institute of Experimental Physics, Slovak Academy of Sciences, Košice, Slovak Republic^{e,f}

¹⁷ School of Physics and Chemistry, University of Lancaster, Lancaster, UK^b

¹⁸ Department of Physics, University of Liverpool, Liverpool, UK^b

¹⁹ Queen Mary and Westfield College, London, UK^b

²⁰ Physics Department, University of Lund, Lund, Sweden^g

²¹ Department of Physics and Astronomy, University of Manchester, Manchester, UK^b

²² CPPM, CNRS/IN2P3 - Univ Mediterranee, Marseille - France

²³ Institute for Theoretical and Experimental Physics, Moscow, Russia

²⁴ Lebedev Physical Institute, Moscow, Russia^{e,h}

²⁵ Max-Planck-Institut für Physik, München, Germany^a

²⁶ LAL, Université de Paris-Sud, IN2P3-CNRS, Orsay, France

²⁷ LPNHE, École Polytechnique, IN2P3-CNRS, Palaiseau, France

²⁸ LPNHE, Universités Paris VI and VII, IN2P3-CNRS, Paris, France

²⁹ Institute of Physics, Academy of Sciences of the Czech Republic, Praha, Czech Republic^{e,i}

³⁰ Faculty of Mathematics and Physics, Charles University, Praha, Czech Republic^{e,i}

³¹ INFN Roma 1 and Dipartimento di Fisica, Università Roma 3, Roma, Italy

³² Paul Scherrer Institut, Villigen, Switzerland

³³ Fachbereich Physik, Bergische Universität Gesamthochschule Wuppertal, Wuppertal, Germany^a

³⁴ Yerevan Physics Institute, Yerevan, Armenia

³⁵ DESY, Zeuthen, Germany^a

³⁶ Institut für Teilchenphysik, ETH, Zürich, Switzerlandⁱ

³⁷ Physik-Institut der Universität Zürich, Zürich, Switzerland^j

³⁸ Present address: Institut für Physik, Humboldt-Universität, Berlin, Germany

³⁹ Also at Rechenzentrum, Bergische Universität Gesamthochschule Wuppertal, Wuppertal, Germany

⁴⁰ Also at Institut für Experimentelle Kernphysik, Universität Karlsruhe, Karlsruhe, Germany

⁴¹ Also at Dept. Fis. Ap. CINVESTAV, Mérida, Yucatán, México^k

⁴² Also at University of P.J. Šafárik, Košice, Slovak Republic

⁴³ Also at CERN, Geneva, Switzerland

† Deceased

^a Supported by the Bundesministerium für Bildung, Wissenschaft, Forschung und Technologie, FRG, under contract numbers 7AC17P, 7AC47P, 7DO55P, 7HH17I, 7HH27P, 7HD17P, 7HD27P, 7KI17I, 6MP17I and 7WT87P

^b Supported by the UK Particle Physics and Astronomy Research Council, and formerly by the UK Science and Engineering Research Council

^c Supported by FNRS-FWO, IISN-IKW

^d Partially Supported by the Polish State Committee for Scientific Research, grant No. 2P0310318 and SPUB/DESY/P-03/DZ 1/99

^e Supported by the Deutsche Forschungsgemeinschaft

^f Supported by VEGA SR grant no. 2/5167/98

^g Supported by the Swedish Natural Science Research Council

^h Supported by Russian Foundation for Basic Research grant no. 96-02-00019

ⁱ Supported by GA AVČR grant number no. A1010821

^j Supported by the Swiss National Science Foundation

^k Supported by CONACyT

1 Introduction

Deep-inelastic scattering (DIS) at the electron-proton collider HERA offers unique possibilities to reveal the partonic structure of matter. At very high four-momentum transfer squared $-Q^2$ the exchange of all the electroweak gauge bosons (photon, Z^0 and W^\pm) becomes important allowing the standard model of electroweak and strong interactions to be tested at distances as small as 10^{-18}m . The inclusive DIS cross sections of neutral current (NC) $ep \rightarrow eX$ and charged current (CC) $ep \rightarrow \nu X$ interactions have been measured [1, 2] and are well described by the standard model. In this analysis we complement these results by the first detailed investigation of dijet structures in both NC and CC processes.

Within the Quark-Parton-Model DIS gives rise to events with (1+1) jets, where one jet originates from a quark struck out of the proton and a second jet is due to the proton remnant (denoted ‘+1’). Events with (2+1) jets, referred to as dijet events, are predicted by Quantum Chromodynamics (QCD) due to contributions in $O(\alpha_s)$, namely QCD-Compton scattering $eq \rightarrow eqg$ and Boson-Gluon-Fusion $eg \rightarrow eq\bar{q}$ as illustrated in Figure 1. In CC interactions several events with multijet structures have been identified [3] and the jet shape has been measured [4]. However, due to the relatively small number of CC events observed so far at HERA, the structure of the hadronic final state has not yet been studied in detail. In NC interactions clear multi-jet structures have been established [5] and have been used to test QCD [6]. Previous analyses of dijet production in NC processes, however, did not yet extend to very high values of Q^2 .

In the present paper a dijet analysis of a sample of 460 CC events and approximately 8 600 NC events with Q^2 in the range of 640 to 35 000 GeV^2 is performed. Various dijet distributions are compared with the predictions of QCD Monte Carlo models and with perturbative QCD calculations in next-to-leading order (NLO). In addition, the jet distributions of the CC and the NC events are compared directly, in order to test the hypothesis that QCD radiation proceeds independently of the underlying electroweak scattering process.

2 Detector description and data selection

This analysis is based on the data sample recorded with the H1 detector in the data taking periods 1994–1997 at HERA. In this period HERA was operated with positron and proton beams of 27.5 and 820 GeV respectively, corresponding to a centre-of-mass energy of $\sqrt{s} \approx 300$ GeV. The collected integrated luminosity for this analysis is 35.6 pb^{-1} .

2.1 Detector and trigger

The components of the H1 detector [7] most relevant for this analysis are the central tracking system, the liquid argon calorimeter and the instrumented iron return yoke.

The central tracking system consists of two concentric drift chambers covering a polar angular range¹ of 15° to 165° . Two polygonal drift chambers with wires perpendicular to the beam

¹The forward direction and the positive z -axis are defined as the proton beam direction. The origin of coordinates is the nominal ep interaction point.

axis improve the determination of the z coordinate of the measured tracks. The central tracking system is surrounded by a liquid argon sampling calorimeter covering a polar angle range of $4^\circ < \theta < 154^\circ$. The electromagnetic and hadronic sections of the liquid argon calorimeter correspond in total to a depth of 4.5 to 8 interaction lengths. The energy resolution of the liquid argon calorimeter for electrons and hadrons was determined in test beam measurements to be $\sigma/E = 12\%/\sqrt{E(\text{GeV})} \oplus 1\%$ and $\sigma/E = 50\%/\sqrt{E(\text{GeV})} \oplus 2\%$, respectively [8]. The systematic uncertainty of the electromagnetic energy scale is determined to be 0.7% for the majority of the selected events and increases to 3% at the highest Q^2 [1]. The uncertainty on the hadronic energy scale of the liquid argon calorimeter is 4%.

Outside the calorimeters a large superconducting solenoid provides a magnetic field of 1.15 Tesla. The instrumented iron return yoke identifies energetic muons and detects leakage of hadronic showers.

The trigger conditions for CC events are based on the reconstruction of a large missing transverse momentum in the trigger sums of the liquid argon calorimeter [9]. NC events are triggered on the basis of a localized high energy deposit in the electromagnetic part of the calorimeter [7].

2.2 Event selection

Selection of CC events

The selection of CC events is similar to those of [1, 10]. It is based on the observation of a large imbalance in transverse momentum due to the antineutrino escaping direct detection. The transverse momentum P_T^{had} , reconstructed with the liquid argon calorimeter and the instrumented iron, is required to exceed 25 GeV. No scattered positron must be found in order to reject neutral current events. The z coordinate of the primary event vertex z_{vtx} has to be within a distance of ± 35 cm from the nominal ep collision point. The inelasticity $y_{had} = \sum_h E_h(1 - \cos \theta_h)/2E_e$, calculated from the energy depositions in the calorimeters and the energy of the positron beam E_e , must be in the range $0.03 < y_{had} < 0.85$. The kinematic selection criteria imply a minimum virtuality Q^2 of the exchanged boson of 640 GeV².

Background events due to cosmic muons, beam-halo muons and beam-gas interactions are removed by further requirements on the event topology and timing [10]. Furthermore a visual scan of the remaining events is performed.

The final event sample consists of 460 CC events. The background from photoproduction events is less than 2%. It is estimated from Monte Carlo simulations and from data events where the scattered electron is detected at very small scattering angles. The number of background events from other sources is negligible.

The trigger efficiency for events with $P_T^{had} > 25$ GeV has been determined as a function of the kinematic variables and the jet variables studied using NC events where the information of the scattered positron [10] is discarded. The average trigger efficiency is $\approx 95\%$. It is corrected for in all measured distributions.

Selection of NC events

The kinematic selection criteria of the NC events correspond to those of the CC events. The

NC selection requires the identification of the scattered positron. Fiducial cuts are applied to the impact position of the scattered positron in the liquid argon calorimeter in order to avoid inhomogeneities at the boundary of detector modules [1]. The kinematic selection is based on the variables p_T^e and y_e reconstructed from the scattered positron momentum with the exception of the requirement $y_{had} > 0.03$. The summed energy E and longitudinal momentum components P_z of all reconstructed detector objects (see section 4.1) must fulfil $E - P_z > 35$ GeV to suppress QED radiative events. The z coordinate of the primary event vertex is required to be in the same range as for the CC events. The NC sample consists of ≈ 8600 events with a negligible number of background events from photoproduction. The trigger efficiency of the NC events is $\approx 99\%$.

The distributions of the reconstructed kinematic variables P_T , Q^2 , the Bjorken scaling variable x and y for the CC and the NC event samples are shown in Figure 2. A good description of the data by the Monte Carlo model ARIADNE (see next section) combined with the H1 detector simulation is observed. Note that the distributions are normalized to the total number of CC or NC events N_{DIS} respectively. The differences between the CC and NC distributions [1] are due to the different couplings and propagators of the bosons in CC and NC interactions.

The main selection criteria for the CC and NC events are summarized in Table 1.

CC	NC
no e^+ found	e^+ found
$P_T^{had} > 25$ GeV	$p_T^e > 25$ GeV
$0.03 < y_{had} < 0.85$	$0.03 < y_{had}, y_e < 0.85$
–	$E - P_z > 35$ GeV
$ z_{vtx} < 35$ cm	$ z_{vtx} < 35$ cm

Table 1: Selection criteria for the CC and NC DIS event samples

3 QCD Monte Carlo models and QCD NLO programs

3.1 QCD Monte Carlo models

Four different QCD Monte Carlo models are used in this analysis: ARIADNE 4.10 [11]; HERWIG 5.9 [12], LEPTO 6.5.2 β [13] and RAPGAP 2.08/06 [14]. All models use the LO matrix elements for QCD-Compton and Boson-Gluon-Fusion. ARIADNE implements higher order QCD processes with radiating colour dipoles [15], HERWIG, LEPTO and RAPGAP use initial and final state parton showers instead [16]. In the context of this analysis LEPTO and RAPGAP are similar. They differ in the way the divergences of the LO matrix element are regulated. Fragmentation of partons into hadrons is modelled with the Lund string model [17] in ARIADNE, LEPTO and RAPGAP, and with the cluster model [18] in HERWIG.

The latest versions of the models as described in [19] are used. The LEPTO version used contains a refinement of soft-colour interactions, the generalised area law model [20]. LEPTO

has been tuned to describe jet distributions at HERA and the corresponding values of the model parameters are taken here. In HERWIG, we use the leading order and not the next-to-leading order formula for α_s as proposed in [19]. The parton density functions CTEQ4L [21] are taken.

ARIADNE and LEPTO are incorporated into DJANGO [22], version 6.2, which simulates the effects of QED radiation.

3.2 QCD NLO programs

Four programs MEPJET [23], DISENT [24], DISASTER++ [25] and JETVIP [26] are available for perturbative QCD calculations of jet cross sections in NLO. Currently MEPJET is the only NLO program that considers W or Z^0 exchange. MEPJET is thus used to calculate the jet distributions in CC processes. The NC jet cross sections are calculated with DISENT following the recommendations in [27]. We use the parton density functions determined by the H1 Collaboration [1] and choose Q^2 as the renormalization and factorization scales, μ_R^2 and μ_F^2 .

We compared the predictions of MEPJET and DISENT for the jet distributions presented below. In leading order, we find agreement within a fraction of a per cent. In NLO, MEPJET is systematically lower than DISENT by $\approx 10\%$ confirming the results of [28]. Note that the comparison of various jet cross sections calculated with DISENT and DISASTER++ showed good agreement [28]. The differences between DISENT and DISASTER++ observed for extreme values of event shape variables [29, 30] are not relevant to this analysis. Currently it is unknown if the inconsistencies between the NLO programs observed in NC influence the CC predictions as well.

DISENT does not consider Z^0 exchange, which for $Q^2 > 5\,000\text{ GeV}^2$ reduces the inclusive e^+p NC cross section by less than 5% on average compared with purely electromagnetic exchange. Since the dijet cross sections are also reduced, the effect on jet distributions normalized to the number of DIS events is small. Correction factors were calculated using ARIADNE 4.10 and are applied to any DISENT prediction at $Q^2 > 5\,000\text{ GeV}^2$.

In order to compare the perturbative QCD predictions to the data, bin-by-bin hadronization corrections are determined using the QCD models ARIADNE and HERWIG. The average correction factors from the two models are applied to the NLO distributions. The maximum deviation between the average correction factor and the correction factor for either model alone is taken as hadronization uncertainty.

4 Definition of jet observables

4.1 Jet algorithm

Jets are reconstructed with a modified version of the Durham jet algorithm which was originally introduced in e^+e^- annihilation experiments [31]. The algorithm is applied in the laboratory frame. It is modified for application in DIS in two respects: a missing-momentum four-vector is introduced which is treated as an additional object by the jet algorithm to account for the

momentum carried by the proton remnant escaping through the beam pipe; in NC events the scattered positron is removed from the final state objects and is only used to determine the missing-momentum vector. In CC events this is achieved by first reconstructing the neutrino from the hadronic final state, exploiting energy and momentum conservation.

The jet algorithm calculates the quantity $k_{T,ij}^2 = 2 \min[E_i^2, E_j^2] (1 - \cos \theta_{ij})$ of pairs of objects or ‘proto’ jets i, j . Here E_i and E_j are the energies of the objects i and j , and θ_{ij} is the angle between them. The jet algorithm combines the pair of objects i, j with the minimum $k_{T,ij}^2$ to be a ‘proto’ jet by adding their four-momenta p_i and p_j . This prescription is repeated iteratively for the remaining objects until exactly (2+1) jets remain. At this stage, every event is treated as a dijet event by definition. Pronounced dijet structures are then selected by imposing a lower limit on y_2 , defined as the minimum $k_{T,ij}^2/W^2$ of any combination of the (2+1) jets. Here, W is the invariant mass of the hadronic final state. It is calculated from all objects entering the jet algorithm.

In order to determine the fraction of events with say (1+1) or (3+1) like jet structures it is more convenient to run the algorithm with a fixed jet resolution parameter y_{cut} . In this case the iterative clustering procedure ends, when the $k_{T,ij}^2/W^2$ of any pair of objects or proto jets is larger than a given value y_{cut} . Thus the number of jets reconstructed varies from event to event.

The algorithm is applied to the tracks reconstructed in the central tracking chambers and the energy depositions (clusters) in the liquid argon calorimeter. For tracks and calorimeter clusters that can be matched, the energy is determined from either the calorimeter alone or from a combination of track and cluster energy as described in [1]. The polar angle of each detector object, track or cluster, is required to exceed 7° in order to avoid the region close to the edge of the calorimeter. This improves the resolution of the reconstructed jet quantities.

The same definitions of the jets are used for the analysis of the data and the Monte Carlo events after detector simulation. In events simulated at the hadron or parton level and in the perturbative QCD calculations, the jet algorithm is applied to hadron or parton four-momenta respectively. The polar angle cut of 7° , which is applied for detector objects, is also applied for hadrons and partons.

In the calculation of y_2 the effects of the hadronic energy scale uncertainty largely cancel due to the method chosen to reconstruct W . The choice of a jet algorithm working in the laboratory frame leads to reduced experimental errors since a boost into another frame is avoided. This is relevant for the CC events where the resolution of the kinematic variables is worse than in NC events.

In the present analysis the jet polar angles must fulfil $10^\circ < \theta_{jet} < 140^\circ$. This restricts the jets to the acceptance of the liquid argon calorimeter.

4.2 Jet observables

The rate of events with jet multiplicity i is defined as $R_i(Q^2) \equiv N_i(Q^2)/N_{DIS}(Q^2)$, where $N_{i=1,2,3}$ is the number of events with one, two or three jets, not counting the proton remnant jet. N_{DIS} is the number of selected deep-inelastic events. The value of y_{cut} is taken as 0.002.

The dijet sample is correspondingly defined by the requirement $y_2 > 0.002$. Large values of y_2 correspond to events with (2+1) jets that are clearly separated and indicative of hard QCD radiation. Small values of y_2 are typical for events which intuitively may be considered as (1+1) jet events. In Figure 3 two CC events with very different values of y_2 are displayed for illustration. Note that, with this definition of the dijet sample, the events contributing to the one-jet rate as introduced above are eliminated, and the few three-jet events are now treated as dijet events.

The distributions of the dijet variables y_2 , m_{12} , z_p , x_p , the polar angle θ_{fwd} and the transverse energy $E_{T,fwd}$ of the most forward (non-remnant) jet are studied. m_{12} is the invariant mass of the two non-remnant jets. The variables z_p and x_p are defined by

$$z_p \equiv \min_{i=1,2} [E_i (1 - \cos \theta_i)] / \sum_{i=1,2} E_i (1 - \cos \theta_i) \quad \text{and} \quad x_p \equiv \frac{Q^2}{Q^2 + m_{12}^2}$$

where E_i and θ_i are the energies and polar angles of the two (non-remnant) jets remaining after the clustering of the jet algorithm. The variable z_p corresponds to $1/2 \min_{i=1,2} (1 - \cos \theta_i^*)$ where θ_i^* is the polar angle of the parton i in the centre-of-mass system of the virtual boson and the incoming parton. In leading order QCD x_p is equal to the ratio x/ξ where ξ is the fraction of the proton's four momentum carried by the parton entering in the hard scattering process (see Figure 1). In the limit where one jet is absorbed into the remnant jet z_p approaches 0. In the other limit, where the two (non-remnant) jets become one jet, m_{12} approaches 0 and x_p approaches 1.

5 Correction of the data

The data are corrected for the effects of detector acceptance and resolution, and of QED radiation using the QCD models ARIADNE and LEPTO. For the correction of CC events, the number of events simulated for either model is approximately 150 times larger than that of the experimental data. The number of simulated NC events is at least six times larger than that of the data. The same event cuts and track/cluster selection criteria are applied to the simulated events and to the data.

Correction of detector effects

The measured jet distributions are corrected for detector effects with bin-by-bin correction factors. The purity, defined as the number of simulated events which originate in a bin and are reconstructed in it, normalized by the number of reconstructed events in that bin, is on average 60% for both CC and NC distributions. The purities estimated with LEPTO and ARIADNE are very similar.

The stability of the results was tested by correcting the jet distributions reconstructed from simulated LEPTO events with the correction factors derived with ARIADNE. The agreement of the corrected jet distributions with the 'true' LEPTO jet distributions is good. Deviations are typically of a few percent. The largest deviations of 10 – 15% are seen in the z_p distribution. These effects are considered in the model uncertainty discussed below.

Correction of QED radiative effects

The effects of QED radiation are considered by correction factors also. These factors are obtained from the ratio of the Monte Carlo distributions generated with and without inclusion of QED effects. The size of the corrections is $\approx 5\%$ for both CC and NC distributions.

The combined detector and QED radiation correction factors from LEPTO and ARIADNE are averaged, and the resulting mean correction factors are used to correct the jet distributions.

6 Determination of systematic errors

The major sources of systematic errors are the model dependence of the detector corrections and the uncertainties of the electromagnetic and the hadronic energy scales of the liquid argon calorimeter. The total error of the majority of the CC data points is dominated by the statistical errors whereas the statistical and systematic errors are roughly of the same size for the NC data.

Model dependence of correction factors

The difference between the (average) corrected distributions and the distributions corrected with either model alone is taken as the error. The error is on average $\approx \pm 3\%$ for both the CC and NC distributions.

Electron energy calibration

The energy scale of electrons measured in the liquid argon calorimeter is known to 0.7% in the angular region where most events are situated. The effect on the jet distributions of the NC event sample is generally smaller than one per cent.

Hadronic energy calibration

In order to estimate the effect of the hadronic energy scale uncertainty on the measured jet distributions, the analysis is repeated with the hadronic cluster energies shifted by $\pm 4\%$. The size of the corresponding changes depends considerably on the observable studied. For the CC events, the largest variation of $\approx 11\%$ is observed for the m_{12} distribution, the smallest variations of $\approx 3\%$ are observed for the y_2 , z_p and θ_{fwd} distributions. Similar variations are observed in the NC jet distributions. A variation of the track momentum by $\pm 3\%$ has negligible effect on the jet distributions.

7 Results

7.1 Jet event rates

The rates of events with one, two and three jets $R_i(Q^2)$ are shown in Figure 4 as a function of Q^2 and are listed in Table 2. The jet event rates for CC and NC events are similar. For the chosen jet resolution, the fraction of one-jet events is $\approx 70\%$ for both CC or NC events. The fraction of dijet events is $\approx 20\%$ and that of three-jet events is a few percent. No CC three-jet events are yet observed at $Q^2 > 5000 \text{ GeV}^2$, which is statistically consistent with the QCD model expectations. The Q^2 dependence of the jet event rates is small. Note that R_1 has a weak Q^2 dependence since most of the DIS events are reconstructed as (1+1) jet events. The jet event rates are well described by the QCD model ARIADNE.

7.2 Differential dijet distributions

The measured CC dijet distributions of y_2 , m_{12} , z_p , x_p , $E_{T, fwd}$ and θ_{fwd} , corrected for detector effects and the effects of QED radiation, are shown in Figure 5. The distributions are based on the 120 CC events that pass the requirements $y_2 > 0.02$ and the $10^\circ < \theta_{fwd} < 140^\circ$. The measured differential dijet cross sections e.g. $d\sigma_{dijet}/dy_2$ are normalized by the inclusive DIS cross section σ_{DIS} for the kinematic selection of section 2. The y_2 and m_{12} distributions are steeply falling. In the tails of these distributions events with clear dijet structures (see Figure 3) and with dijet masses up to ≈ 100 GeV are observed. The z_p distribution shows a drop in the first bin at small z_p which is due to the jet selection cut. The x_p distribution is strongly peaked at large values of x_p because the minimum Q^2 of the event selection is large. The corresponding average value of ξ is ≈ 0.1 . The forward jet distributions are strongly increasing at small polar angles and small transverse energies as is qualitatively expected by gluon bremsstrahlung off an incoming quark.

In Figure 6 the corresponding distributions are shown for NC events. Here ≈ 1900 events remain after the jet selection. The NC distributions show the same features as the CC distributions. Note that due to the reduced statistical error of the NC distributions their total error is much smaller than that of the CC distributions. The differential CC and NC dijet distributions presented here are listed in Tables 3.

The corrected jet distributions are compared with the QCD models ARIADNE, HERWIG, LEPTO and RAPGAP. Within the errors, the data are reasonably well described by the QCD models ARIADNE, HERWIG and RAPGAP. LEPTO roughly follows the data distributions but overall it is inferior to the other models. Significant deviations from the data are observed in the z_p distribution in particular. These observations are valid for both CC and NC distributions.

7.3 Comparison with perturbative QCD calculations in NLO

The differential dijet distributions are also compared with QCD predictions in NLO. Two sources of theoretical error on the QCD predictions have been considered: the uncertainty of the hadronization corrections and the renormalization scale uncertainties. The size of these uncertainties is similar for CC and NC events. The hadronization corrections are typically smaller than 10%. Their uncertainty is estimated by the spread of the predictions of ARIADNE and HERWIG. The renormalization scale uncertainty of the NLO prediction is estimated by varying the renormalization scale μ_R^2 from Q^2 to $1/4 Q^2$ and $4 Q^2$. The resulting uncertainty is $\approx 5\%$. The non-remnant jets' average transverse energy in the Breit frame $\langle E_T^{Breit} \rangle$ is ≈ 10 GeV. Choosing $\langle E_T^{Breit} \rangle^2$ as renormalization scale changes the NLO predictions by $\approx 5\%$ compared with the scale Q^2 . A variation of the factorization scale has a marginal effect.

The CC jet distributions are compared with the NLO calculations of MEPJET in Figure 7. The MEPJET predictions provide a reasonable description of the data within errors. The corresponding NC distributions shown in Figure 8 are well described by the NLO predictions of DISENT.

In the Figures 7 and 8 the NLO predictions for quark- and gluon-induced processes are also shown separately². The predicted fraction of gluon-induced dijet events is $\approx 20\%$ in CC and $\approx 15\%$ in NC scattering for the selection criteria of this analysis. These fractions change by less than one per cent when varying the factorization or renormalization scale in the QCD calculations from Q^2 to $1/4$ and $4 Q^2$. The dominance of quark-induced processes is mostly due to the relatively large values of x covered in this analysis. Figure 7 suggests that both quark and gluon contributions – calculated using the parton density functions determined from inclusive measurements – are needed to give a consistent description of dijet production in CC processes.

The CC and NC jet distributions have also been determined for the subsample of the selected DIS events with $Q^2 > 5\,000 \text{ GeV}^2$. After the jet cuts 17 CC and 91 NC dijet events remain. In Figure 9 the corresponding dijet mass distributions are compared with the NLO predictions of MEPJET and DISENT. Agreement is found in all bins. The measured distributions are also listed in Table 4.

7.4 Direct comparison of CC and NC dijet distributions

In Figure 10 the jet distributions of the CC events (full circles) are compared with those of the NC events selected in the same kinematic range (histogram). Systematic differences between the jet distributions are observed in several bins. This is expected due to the different electroweak couplings and gauge boson propagators which also lead to different kinematic distributions (see Figure 2). In order to account for these effects and to make possible a direct, model independent comparison of jet production in CC and NC processes, the NC events are reweighted to match the x and Q^2 spectra of the CC events. The weights are given by the ratio of the inclusive NC and CC DIS cross sections at the x and Q^2 of the NC event considered. The cross sections are calculated with DJANGO, and QED radiative corrections are taken into account. Note that the inclusive cross sections do not depend on the hadronic final state properties and thus the reweighting procedure is independent of the modelling of the hadronic final state.

The effect of this procedure has been tested with the QCD models ARIADNE, HERWIG and RAPGAP, and the jet distributions of CC and reweighted NC events are predicted to agree within a few per cent typically. Residual differences between CC and reweighted NC jet distributions are expected due to the different fraction of gluon induced events in CC and NC processes, to helicity effects [33, 34], and to the different parton densities contributing to NC and CC scattering. The NC event selection was repeated with the cut $P_T^{had} > 25 \text{ GeV}$ instead of $p_T^e > 25 \text{ GeV}$. The changes in the corrected jet distributions are of the order of 2%.

The measured NC jet distributions after reweighting are also shown in Figure 10. They are found to be consistent with the CC distributions confirming that at short distances the QCD dynamics of the hadronic final state are essentially independent of the underlying electroweak scattering process as is expected within the standard model.

²Note that the normalizations σ_{DIS} of the quark-induced, gluon-induced and combined dijet cross sections are identical.

8 Summary

A sample of 460 CC and of $\approx 8\,600$ NC events produced in deep-inelastic e^+p scattering at HERA with the boson virtuality ranging from approximately $640 < Q^2 < 35\,000 \text{ GeV}^2$ has been selected. In this sample jets are reconstructed using a modified version of the Durham algorithm. Jet studies are hence extended into a kinematic region where charged and neutral gauge bosons contribute at comparable level.

Events with dijet structures are observed in CC processes. Differential CC dijet distributions are measured for the first time. Perturbative QCD calculations in NLO based on the MEPJET program describe the data well within errors. These calculations suggest that both quark and gluon contributions are needed to give a consistent description of dijet production in CC processes. The NC dijet distributions, measured in the same kinematic range, are well described by perturbative QCD predictions in NLO based on DISENT.

The measured data sample contains events up to $Q^2 \approx 35\,000 \text{ GeV}^2$ and $m_{12} \approx 100 \text{ GeV}$ and therefore probes QCD down to shortest distances. Using parton densities derived from NLO QCD fits to inclusive DIS cross sections, perturbative calculations based on the electroweak and the strong ($O(\alpha_s^2)$) matrix elements are found to give a consistent description of both the NC and CC jet cross sections at highest dijet masses and highest Q^2 .

Comparison of the CC with the NC jet distributions confirms that at short distances the QCD dynamics of the hadronic final state are essentially independent of the underlying electroweak scattering process as is expected within the standard model.

Acknowledgements

We are very grateful to the HERA machine group whose outstanding efforts made this experiment possible. We acknowledge the support of the DESY technical staff. We appreciate the big effort of the engineers and technicians who constructed and maintain the detector. We thank the funding agencies for financial support of this experiment. We wish to thank the DESY directorate for the support and hospitality extended to the non-DESY members of the collaboration.

References

- [1] H1 Collaboration, C. Adloff *et al.*, Eur. Phys. J. **C13** (2000) 609.
- [2] ZEUS Collaboration, J. Breitweg *et al.*, Eur. Phys. J. **C11** (1999) 427;
ZEUS Collaboration, J. Breitweg *et al.*, Eur. Phys. J. **C12** (2000) 411.
- [3] ZEUS Collaboration, M. Derrick *et al.*, Z. Phys. **C72** (1996) 47.
- [4] ZEUS Collaboration, J. Breitweg *et al.*, Eur. Phys. J. **C8** (1999) 367.
- [5] H1 Collaboration, I. Abt *et al.*, Z. Phys. **C61** (1994) 59;
ZEUS Collaboration, M. Derrick *et al.*, Z. Phys. **C67** (1995) 81.

- [6] see e.g. ZEUS Collaboration, M. Derrick *et al.*, Phys. Lett. **B363** (1995) 201;
H1 Collaboration, C. Adloff *et al.*, Eur. Phys. J. **C6** (1999), 575;
H1 Collaboration, C. Adloff *et al.*, Eur. Phys. J. **C5** (1998), 625;
H1 Collaboration, C. Adloff *et al.*, Eur. Phys. J. **C13** (2000) 415.
- [7] H1 Collaboration, I. Abt *et al.*, Nucl. Instr. and Meth. **A386** (1997) 310 and 348.
- [8] H1 Calorimeter Group, B. Andrieu *et al.*, Nucl. Instr. and Meth. **A336** (1993) 499;
H1 Calorimeter Group, B. Andrieu *et al.*, Nucl. Instr. and Meth. **A350** (1994) 57.
- [9] H1 Calorimeter Group, B. Andrieu *et al.*, Nucl. Instr. and Meth. **A336** (1993) 460.
- [10] H1 Collaboration, S. Aid *et al.*, Phys.Lett. **B379** (1996) 319;
E. Chabert, Ph.D. thesis, University of Marseille, *in preparation*;
I. Negri, Ph.D. thesis, University of Marseille (1998).
- [11] L. Lönnblad, Comp. Phys. Comm. **71** (1992) 15.
- [12] G. Marchesini *et al.*, Comp. Phys. Comm. **67** (1992) 465.
- [13] G. Ingelman, A. Edin and J. Rathsman, Comp. Phys. Comm. **101** (1997) 108.
- [14] H. Jung, Comp. Phys. Comm. **86** (1995) 147;
RAPGAP program manual (1998) unpublished.
- [15] G. Gustafson, Phys. Lett. **B175** (1986) 453;
G. Gustafson and U. Pettersson, Nucl. Phys. **B306** (1988) 746;
B. Andersson, G. Gustafson L. Lönnblad and U. Pettersson, Z. Phys. **C43** (1989) 625.
- [16] M. Bengtsson and T. Sjöstrand, Z.Phys. **C37** (1988) 465.
- [17] B. Andersson *et al.*, Phys. Rep. **97** (1983) 31;
T. Sjöstrand and M. Bengtsson, Comp. Phys. Comm. **43** (1987) 367.
- [18] B.R. Webber, Nucl. Phys. **B238** (1984) 492.
- [19] N.H. Brook, T. Carli, E. Rodrigues, M.R. Sutton, N. Tobien and M. Weber, Proceedings
of the Workshop *Monte Carlo Generators for HERA Physics*, Eds. A.T. Doyle, G. Grind-
hammer, G. Ingelman and H. Jung, DESY-PROC-1999-02 10 and hep-ex/9912053.
- [20] J. Rathsman, Phys. Lett. **B452** (1999) 364.
- [21] CTEQ Collaboration, H.L. Lai *et al.*, Phys. Rev. **D55** (1997) 1280.
- [22] G.A. Schuler and H. Spiesberger, Proceedings of the Workshop *Physics at HERA*, Eds.
W. Buchmüller and G. Ingelman, Vol. 3 (1991) 1419.
- [23] E. Mirkes and D. Zeppenfeld, Phys. Lett. **B380** (1996) 205.
- [24] S. Catani and M.H. Seymour, Nucl. Phys. **B485** (1997) 291.
- [25] D. Graudenz, hep-ph/9710244.

- [26] B. Pötter, *Comp. Phys. Comm.* **119** (1999) 45.
- [27] D. Graudenz and M. Weber, Proceedings of the Workshop *Monte Carlo Generators for HERA Physics*, Eds. A.T. Doyle, G. Grindhammer, G. Ingelman and H. Jung, DESY-PROC-1999-02 117.
- [28] C. Duprel, Th. Hadig, N. Kauer and M. Wobisch, Proceedings of the Workshop *Monte Carlo Generators for HERA Physics*, Eds. A.T. Doyle, G. Grindhammer, G. Ingelman and H. Jung, DESY-PROC-1999-02 142 and hep-ph/9910448.
- [29] G. McCance, Proceedings of the Workshop *Monte Carlo Generators for HERA Physics*, Eds. A.T. Doyle, G. Grindhammer, G. Ingelman and H. Jung, DESY-PROC-1999-02 151 and hep-ph/9912481.
- [30] V. Antonelli, M. Dasgupta and G. Salam, *J. High Energy Phys.* 02 (2000) 001 and hep-ph/9912488.
- [31] S. Catani *et al.*, *Phys. Lett.* **B269** (1991) 432.
- [32] T. Brodtkorb, J.G. Körner, E. Mirkes, G.A. Schuler, *Z. Phys.* **C44** (1989) 415;
D. Graudenz, N. Magnussen, Proceedings of the Workshop *Physics at HERA*, Eds. W. Buchmüller and G. Ingelman, DESY (1991) 261.
- [33] J.G. Körner, E. Mirkes and G.A. Schuler, *Int. J. Mod. Phys.* **A4** (1989) 1781;
E. Mirkes, TTP-97-39, University of Karlsruhe and hep-ph/9711224.
- [34] M. H. Seymour, *Nucl. Phys.* **B436** (1995) 443.

	CC			NC		
Q^2 [GeV] ²	$R_1(Q^2)$	δ_{stat} (%)	δ_{sys} (%)	$R_1(Q^2)$	δ_{stat} (%)	δ_{sys} (%)
600 – 2000	0.64	±11	±1	0.69	±2.2	±1.0
2000 – 5000	0.71	±12	±1	0.71	±4.5	±0.9
> 5000	0.76	±18	±1	0.70	±9.3	±1.1
Q^2 [GeV] ²	$R_2(Q^2)$	δ_{stat} (%)	δ_{sys} (%)	$R_2(Q^2)$	δ_{stat} (%)	δ_{sys} (%)
600 – 2000	0.21	±16	±1	0.172	±3.5	±2.5
2000 – 5000	0.25	±17	±2	0.22	±6.7	±2.0
> 5000	0.24	±27	±2	0.26	±13	±2
Q^2 [GeV] ²	$R_3(Q^2)$	δ_{stat} (%)	δ_{sys} (%)	$R_3(Q^2)$	δ_{stat} (%)	δ_{sys} (%)
600 – 2000	0.022	±37	±5	0.012	±11	±11
2000 – 5000	0.013	±61	±6	0.02	±20	±8
> 5000	0.0	+0.016 (68% CL)	–	0.028	±35	±9

Table 2: Rates of CC and NC events with one, two and three jets as a function of Q^2 . The events satisfy $p_T^{lept} > 25$ GeV and $0.03 < y < 0.85$. The jets are reconstructed using the modified Durham algorithm with a fixed jet resolution parameter $y_{cut} = 0.002$. The jets satisfy the cut $10^\circ < \theta_{jet} < 140^\circ$. The relative statistical errors δ_{stat} and relative systematic errors δ_{sys} are given in per cent.

	CC			NC		
y_2	$\frac{1}{\sigma_{DIS}} \frac{d\sigma_{dijet}}{dy_2}$	$\delta_{stat}(\%)$	$\delta_{sys}(\%)$	$\frac{1}{\sigma_{DIS}} \frac{d\sigma_{dijet}}{dy_2}$	$\delta_{stat}(\%)$	$\delta_{sys}(\%)$
0.002 – 0.006	33	± 13	± 2	31.4	± 3.5	± 3.1
0.006 – 0.014	10	± 17	± 2	6.3	± 5.4	± 2.8
0.014 – 0.05	0.7	± 28	± 3	0.56	± 8.9	± 6.1
m_{12} [GeV]	$\frac{1}{\sigma_{DIS}} \frac{d\sigma_{dijet}}{dm_{12}}$ [GeV $^{-1}$]	$\delta_{stat}(\%)$	$\delta_{sys}(\%)$	$\frac{1}{\sigma_{DIS}} \frac{d\sigma_{dijet}}{dm_{12}}$ [GeV $^{-1}$]	$\delta_{stat}(\%)$	$\delta_{sys}(\%)$
5 – 20	0.005	± 17	± 4	0.0067	± 4.0	± 3.9
20 – 40	0.006	± 14	± 2	0.0036	± 4.5	± 3.9
40 – 65	0.0016	± 23	± 5	0.0008	± 9	± 10
65 – 120	0.0002	± 53	± 12	0.00008	± 18	± 15
z_p	$\frac{1}{\sigma_{DIS}} \frac{d\sigma_{dijet}}{dz_p}$	$\delta_{stat}(\%)$	$\delta_{sys}(\%)$	$\frac{1}{\sigma_{DIS}} \frac{d\sigma_{dijet}}{dz_p}$	$\delta_{stat}(\%)$	$\delta_{sys}(\%)$
0. – 0.1	0.27	± 29	± 5	0.18	± 9.4	± 7.0
0.1 – 0.2	0.47	± 22	± 11	0.47	± 5.7	± 4.1
0.2 – 0.5	0.56	± 12	± 3	0.44	± 3.4	± 2.4
x_p	$\frac{1}{\sigma_{DIS}} \frac{d\sigma_{dijet}}{dx_p}$	$\delta_{stat}(\%)$	$\delta_{sys}(\%)$	$\frac{1}{\sigma_{DIS}} \frac{d\sigma_{dijet}}{dx_p}$	$\delta_{stat}(\%)$	$\delta_{sys}(\%)$
0. – 0.6	0.077	± 21	± 2	0.066	± 6.2	± 9.9
0.6 – 0.8	0.36	± 17	± 3	0.31	± 4.9	± 3.1
0.8 – 0.9	0.81	± 16	± 3	0.57	± 5.0	± 4.7
0.9 – 1.0	0.41	± 26	± 6	0.39	± 6.6	± 9.0
$E_{T,fwd}$ [GeV]	$\frac{1}{\sigma_{DIS}} \frac{d\sigma_{dijet}}{dE_{T,fwd}}$ [GeV $^{-1}$]	$\delta_{stat}(\%)$	$\delta_{sys}(\%)$	$\frac{1}{\sigma_{DIS}} \frac{d\sigma_{dijet}}{dE_{T,fwd}}$ [GeV $^{-1}$]	$\delta_{stat}(\%)$	$\delta_{sys}(\%)$
4 – 15	0.0088	± 15	± 2	0.0094	± 3.9	± 3.7
15 – 35	0.0057	± 14	± 2	0.0041	± 4.4	± 5.7
35 – 80	0.00067	± 26	± 7	0.00029	± 10	± 15
θ_{fwd} [deg]	$\frac{1}{\sigma_{DIS}} \frac{d\sigma_{dijet}}{d\theta_{fwd}}$ [deg $^{-1}$]	$\delta_{stat}(\%)$	$\delta_{sys}(\%)$	$\frac{1}{\sigma_{DIS}} \frac{d\sigma_{dijet}}{d\theta_{fwd}}$ [deg $^{-1}$]	$\delta_{stat}(\%)$	$\delta_{sys}(\%)$
10 – 20	0.013	± 13	± 2	0.0118	± 3.7	± 4.2
20 – 35	0.0043	± 17	± 2	0.0035	± 5.3	± 1.7
35 – 90	0.00086	± 23	± 3	0.0005	± 7.7	± 3.4

Table 3: Normalized dijet cross sections as a function of y_2 , m_{12} , z_p , x_p , $E_{T,fwd}$ and θ_{fwd} in CC and NC events with $p_T^{lept} > 25$ GeV and $0.03 < y < 0.85$ determined with the modified Durham algorithm. The events satisfy the cuts $y_2 > 0.002$ and $10^\circ < \theta_{jet} < 140^\circ$. The relative statistical errors δ_{stat} and systematic errors δ_{sys} are given in per cent.

m_{12} [GeV]	CC			NC		
	$\frac{1}{\sigma_{DIS}} \frac{d\sigma_{dijet}}{dm_{12}}$ [GeV ⁻¹]	$\delta_{stat}(\%)$	$\delta_{sys}(\%)$	$\frac{1}{\sigma_{DIS}} \frac{d\sigma_{dijet}}{dm_{12}}$ [GeV ⁻¹]	$\delta_{stat}(\%)$	$\delta_{sys}(\%)$
5 – 20	0.0016	±102	±11	0.0045	±28	±8
20 – 40	0.0054	±38	±4	0.0076	±15	±2
40 – 65	0.0033	±43	±4	0.0021	±26	±2
65 – 120	0.00052	±74	±7	0.00039	±39	±14

Table 4: Normalized dijet cross sections as a function of m_{12} in CC and NC events with $Q^2 > 5000 \text{ GeV}^2$, $p_T^{lept} > 25 \text{ GeV}$ and $0.03 < y < 0.85$ determined with the modified Durham algorithm. The events satisfy the cuts $y_2 > 0.002$ and $10^\circ < \theta_{jet} < 140^\circ$. The relative statistical errors δ_{stat} and systematic errors δ_{sys} are given in per cent.

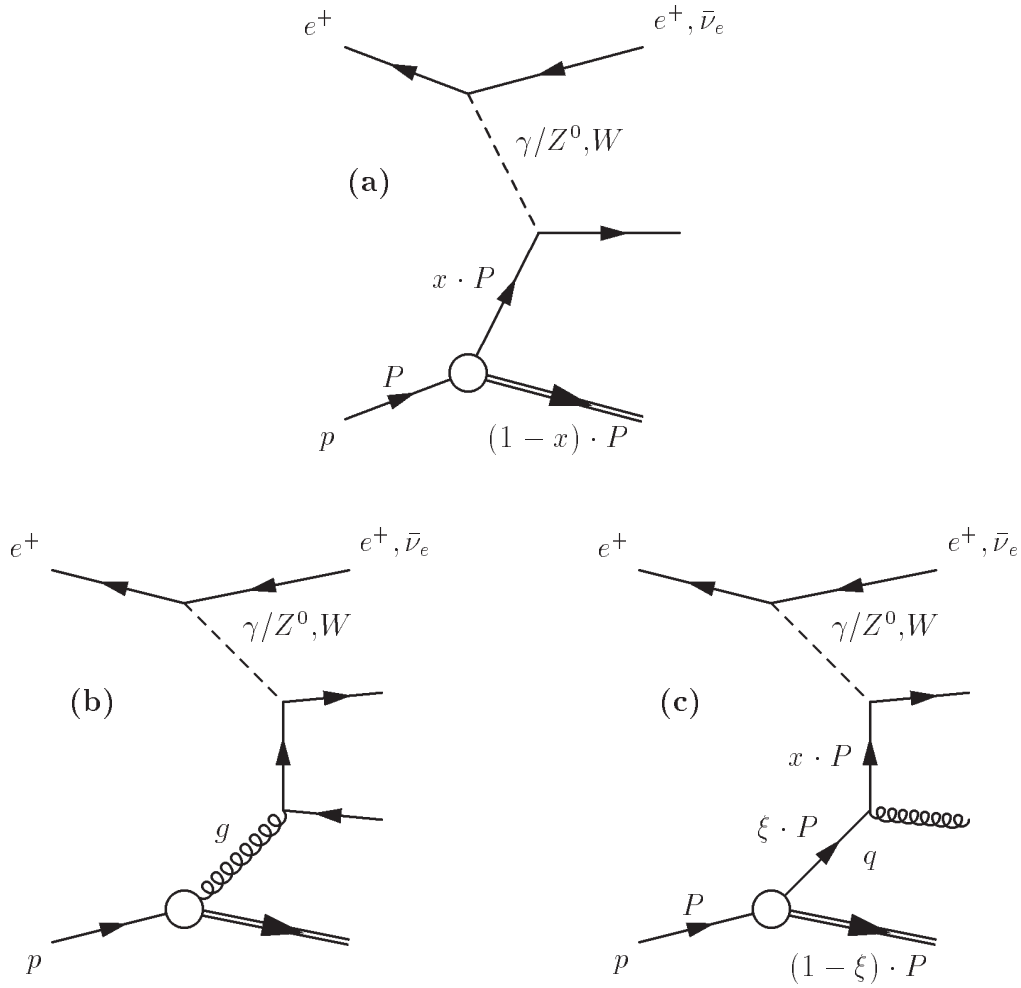


Figure 1: Feynman graphs for DIS in lowest order (a), and selected leading-order diagrams contributing to dijet production: Boson-Gluon-Fusion (b) and QCD-Compton scattering (c). The variables x and ξ denote the fraction of the proton's momentum P carried by the scattered parton.

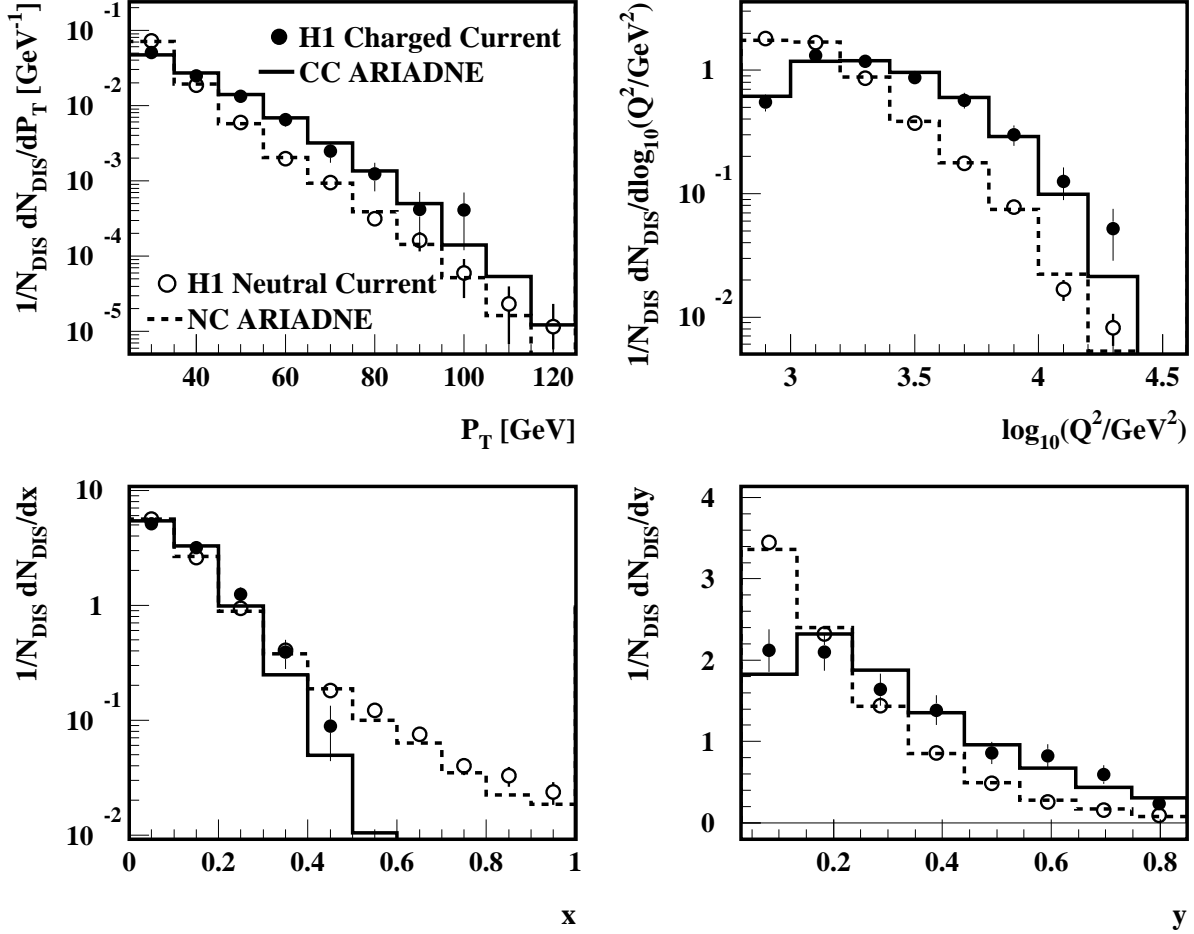


Figure 2: Uncorrected data distributions of P_T , Q^2 , x and y for the selected CC and NC events. The observables are calculated using the hadronic final state for CC events, and the scattered positron for NC events. The errors are statistical only. Also shown are the corresponding predictions of the MC model ARIADNE 4.10 including radiative QED corrections and the H1 detector simulation for CC processes (full line) and NC processes (dashed).

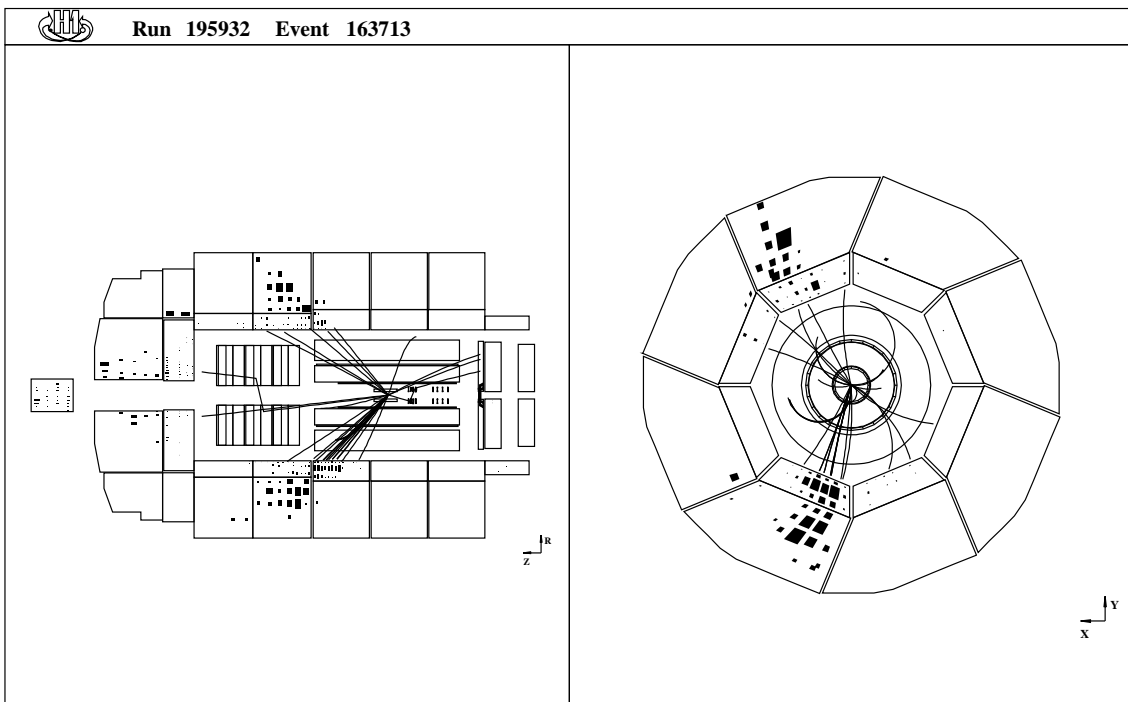
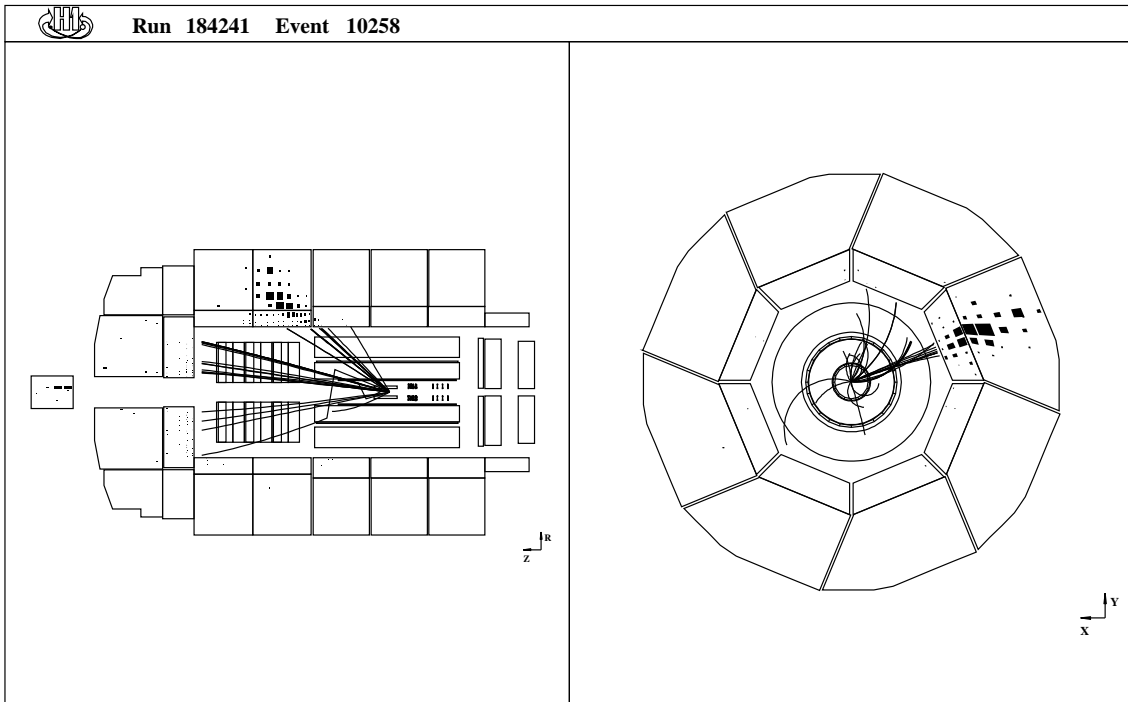


Figure 3: A display of two CC events. The left part shows a side view of the H1 central and forward tracking systems surrounded by the electromagnetic and hadronic sections of the liquid argon calorimeter and of the lead/scintillating-fibre calorimeter. The full lines and filled rectangles correspond to tracks reconstructed in the tracking systems and energy depositions in the calorimeter, respectively. The proton beam enters from the right. The right part shows a view along the beam of the same events. For the upper event $y_2 \approx 0.00008$ and $m_{12} \approx 12$ GeV. For the the lower event $y_2 \approx 0.013$ and $m_{12} \approx 73$ GeV.

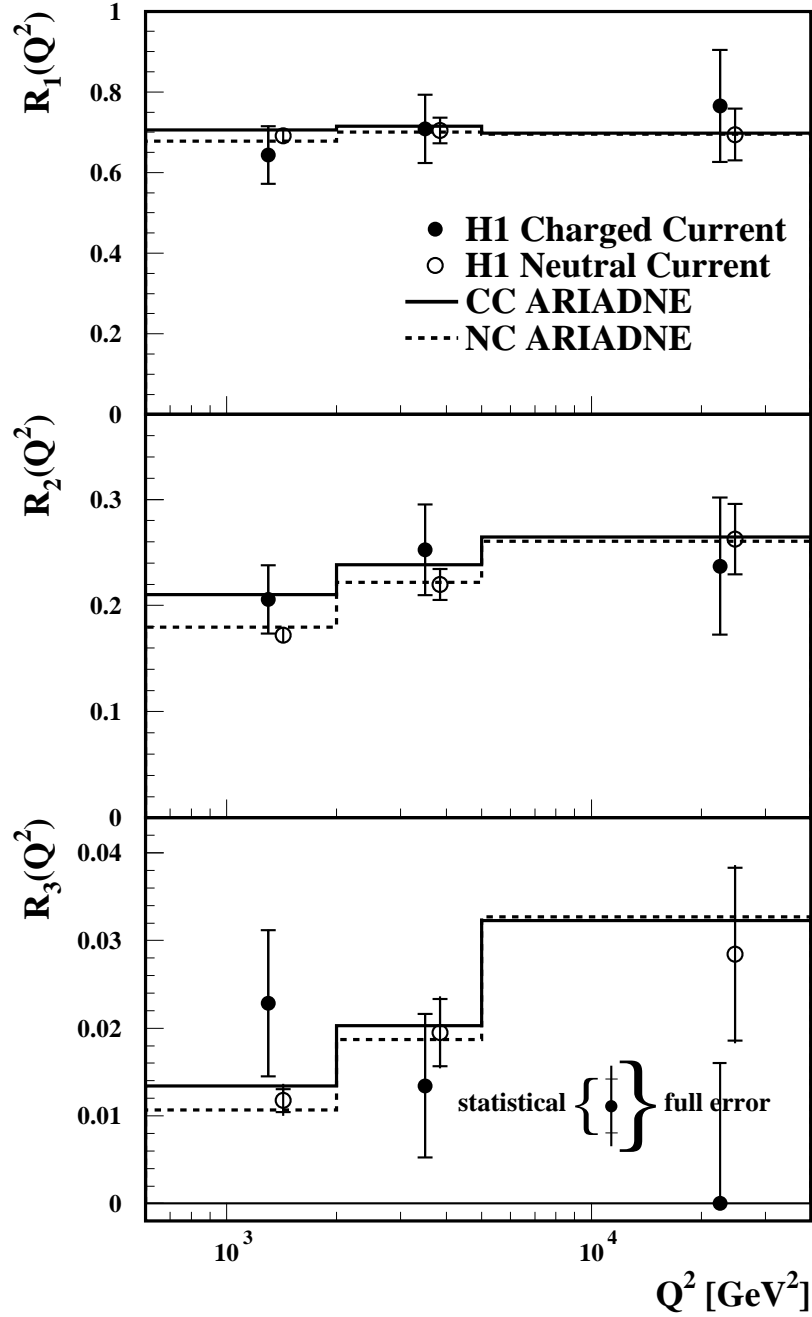


Figure 4: Rates of CC and NC events with one, two and three jets as a function of Q^2 . The events satisfy $p_T^{lept} > 25$ GeV and $0.03 < y < 0.85$. The jets are reconstructed using the modified Durham algorithm with a fixed jet resolution parameter $y_{cut} = 0.002$. The jets satisfy the cut $10^\circ < \theta_{jet} < 140^\circ$. Also shown are the predictions of the MC model ARIADNE 4.10.

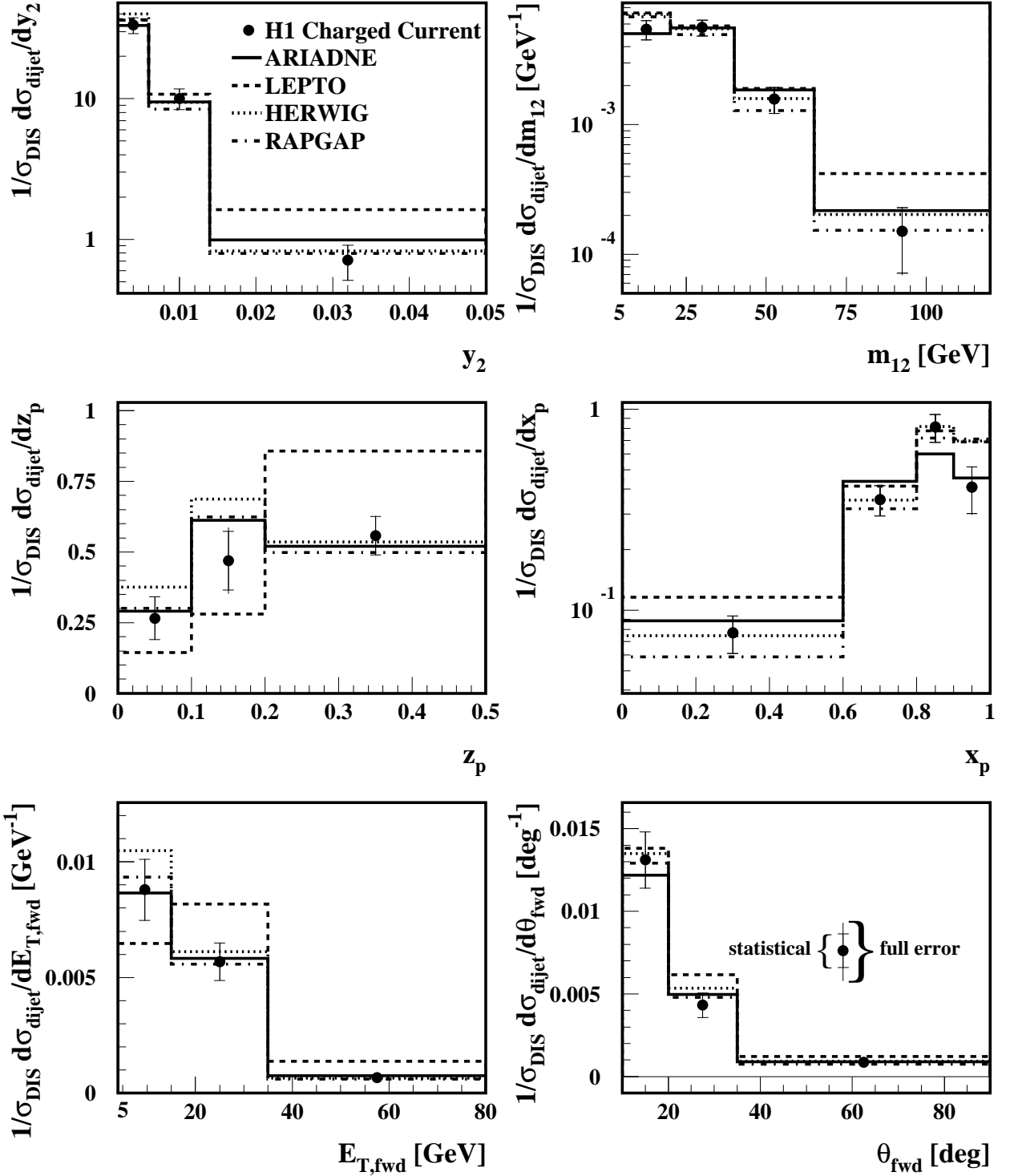


Figure 5: Distributions of y_2 , m_{12} , z_p , x_p , $E_{T,fwd}$ and θ_{fwd} in CC events with $p_T^{lept} > 25$ GeV and $0.03 < y < 0.85$ determined with the modified Durham algorithm. The events satisfy the cuts $y_2 > 0.002$ and $10^\circ < \theta_{jet} < 140^\circ$. Also shown are the predictions of the MC models ARIADNE 4.10 (full line), LEPTO 6.5.2 β (dashed), HERWIG 5.9 (dotted) and RAPGAP 2.08/06 (dashed-dotted).

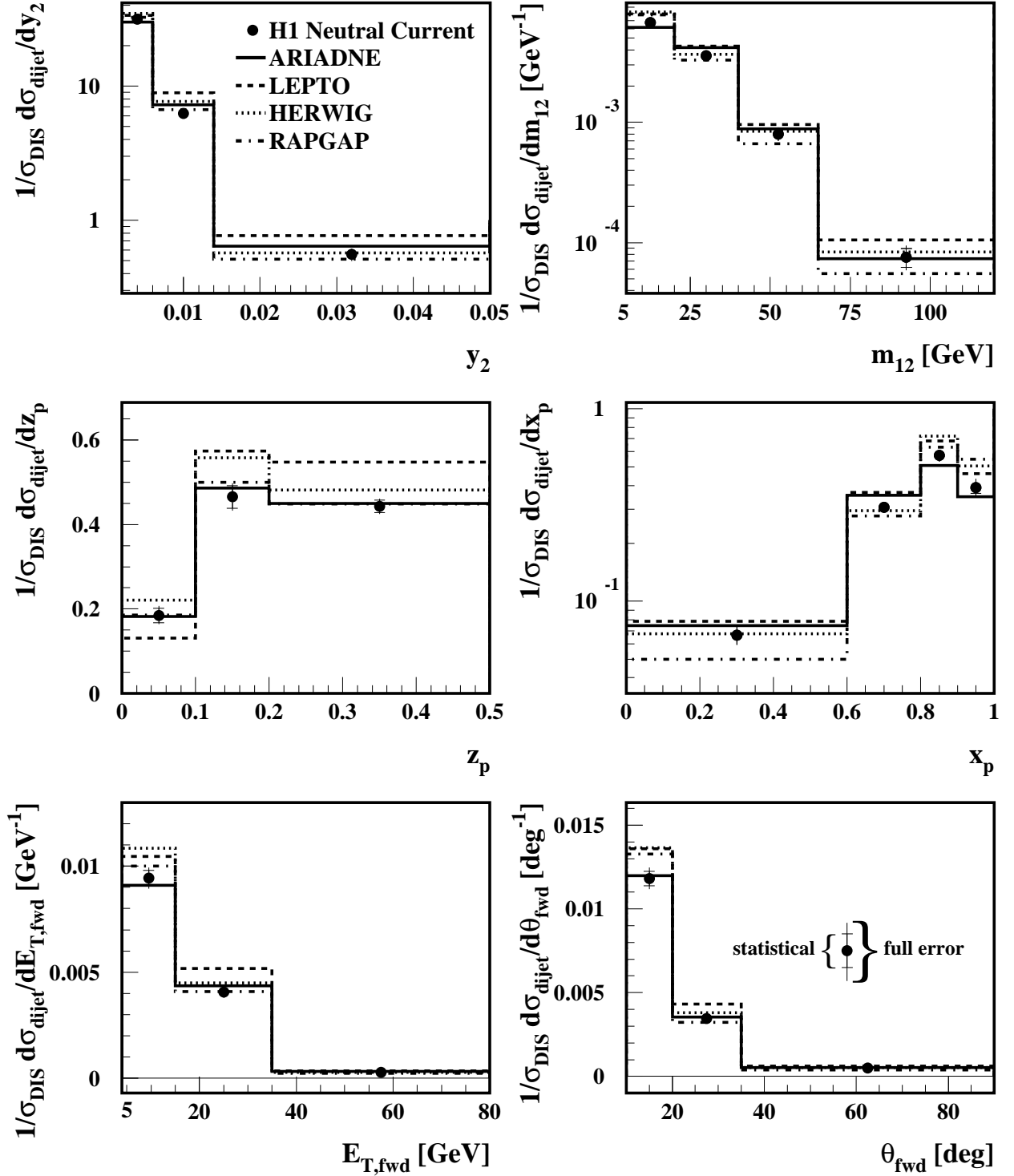


Figure 6: Distributions of y_2 , m_{12} , z_p , x_p , $E_{T,fwd}$ and θ_{fwd} in NC events with $p_T^{lept} > 25$ GeV and $0.03 < y < 0.85$ determined with the modified Durham algorithm. The events satisfy the cuts $y_2 > 0.002$ and $10^\circ < \theta_{jet} < 140^\circ$. Also shown are the predictions of the MC models ARIADNE 4.10 (full line), LEPTO 6.5.2 β (dashed), HERWIG 5.9 (dotted) and RAPGAP 2.08/06 (dashed-dotted).

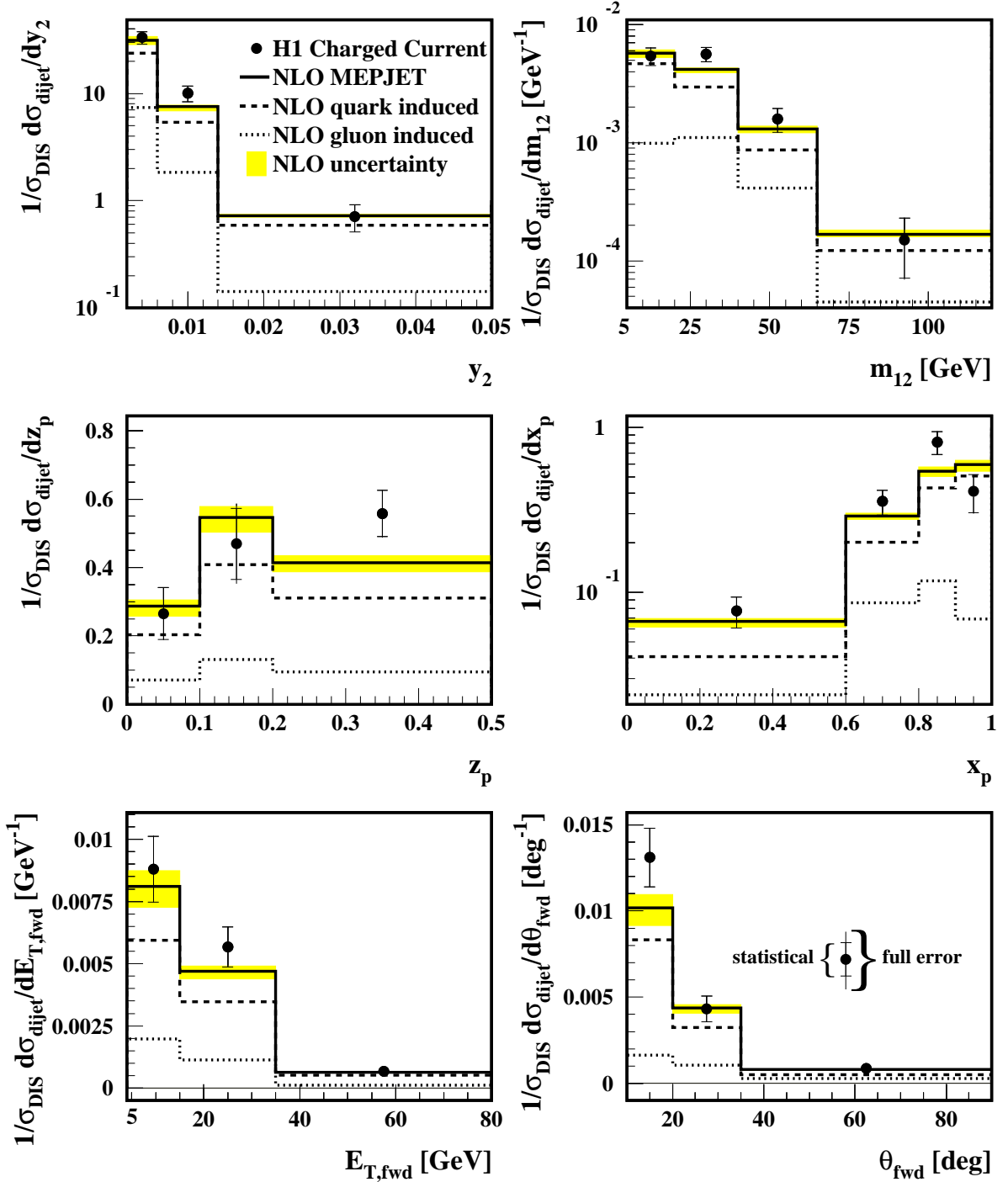


Figure 7: Distributions of y_2 , m_{12} , z_p , x_p , $E_{T, fwd}$ and θ_{fwd} in CC events with $p_T^{lept} > 25$ GeV and $0.03 < y < 0.85$ determined with the modified Durham algorithm. The events satisfy the cuts $y_2 > 0.002$ and $10^\circ < \theta_{jet} < 140^\circ$. Also shown are perturbative QCD calculations in NLO obtained with MEPJET combined with a correction for hadronization effects. The shaded area shows the hadronization uncertainties and the renormalization scale uncertainties of the NLO calculations added in quadrature. In addition, the jet distributions obtained for quark- and gluon-induced processes are shown separately.

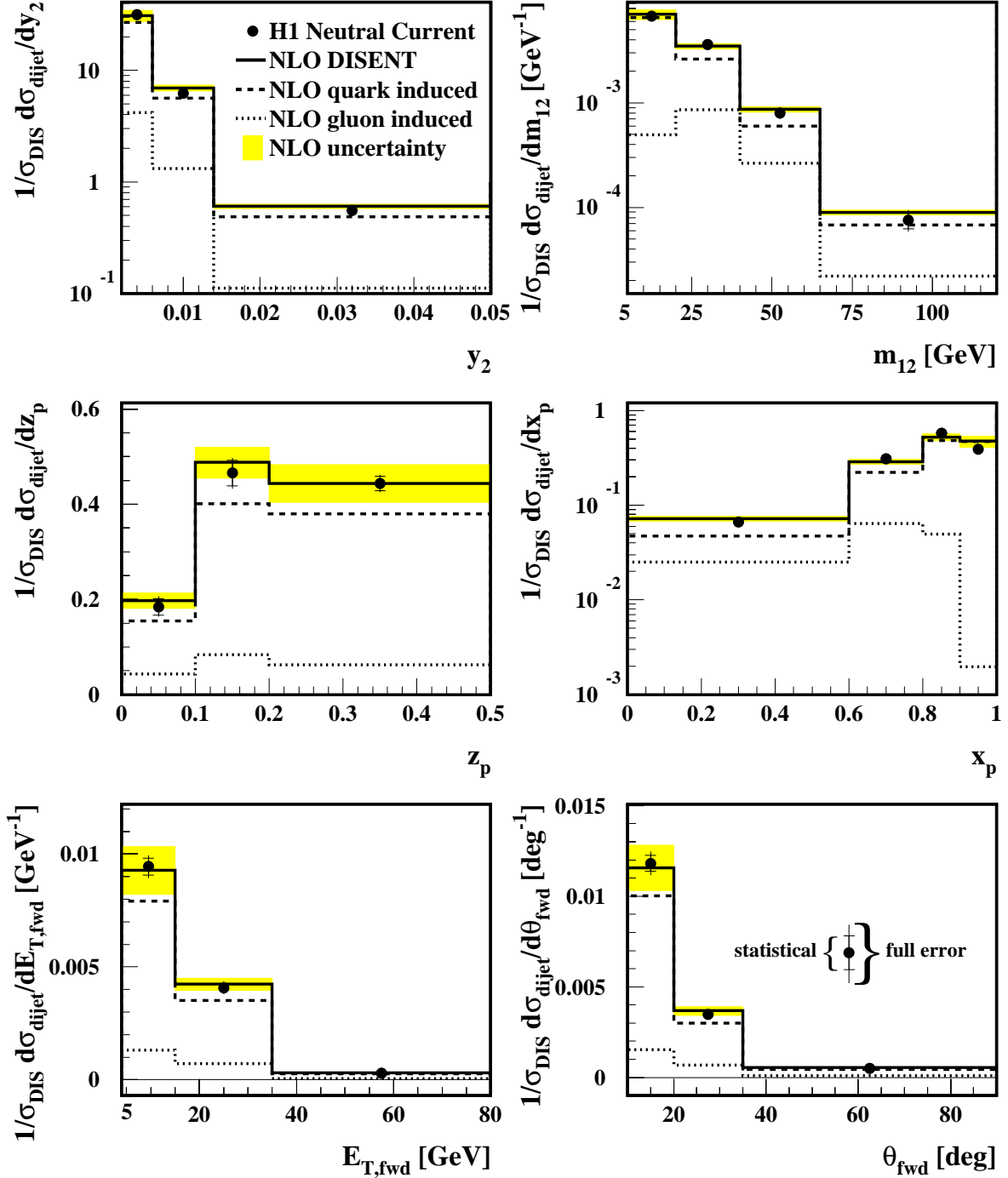


Figure 8: Distributions of y_2 , m_{12} , z_p , x_p , $E_{T, fwd}$ and θ_{fwd} in NC events with $p_T^{lept} > 25$ GeV and $0.03 < y < 0.85$ determined with the modified Durham algorithm. The events satisfy the cuts $y_2 > 0.002$ and $10^\circ < \theta_{jet} < 140^\circ$. Also shown are perturbative QCD calculations in NLO obtained with DISENT combined with a correction for hadronization effects. The shaded area shows the hadronization uncertainties and the renormalization scale uncertainties of the NLO calculations added in quadrature. In addition, the jet distributions obtained for quark- and gluon-induced processes are shown separately.

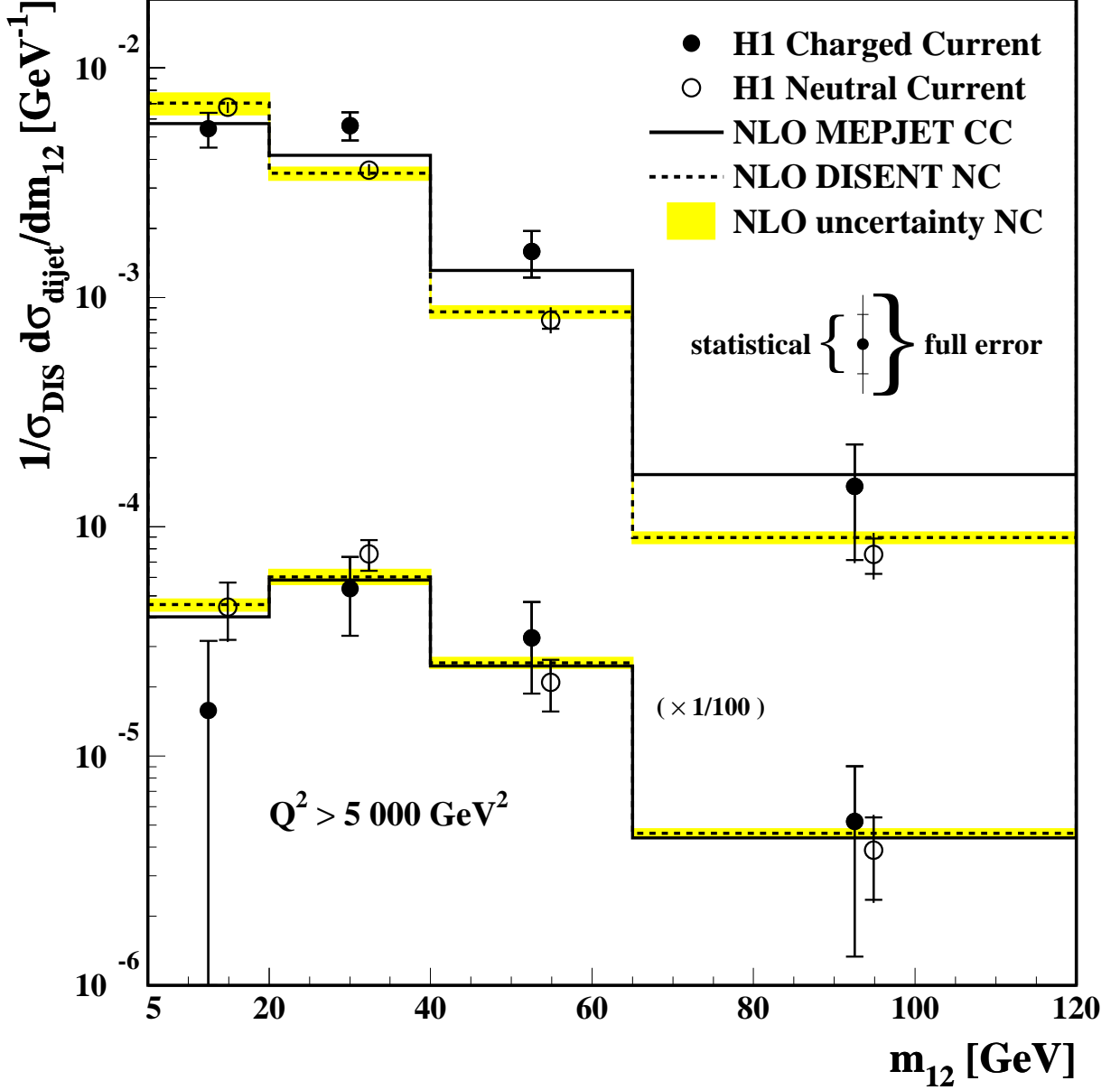


Figure 9: Distributions of m_{12} in CC events (full circles) and NC events (empty circles) for $p_T^{lept} > 25$ GeV and $0.03 < y < 0.85$ with and without the additional requirement $Q^2 > 5000$ GeV² determined with the modified Durham algorithm. The events satisfy the cuts $y_2 > 0.002$ and $10^\circ < \theta_{jet} < 140^\circ$. Also shown are perturbative QCD calculations in NLO obtained with MEPJET (for CC) and DISENT (for NC) combined with a correction for hadronization effects. The lower histograms and the corresponding data points have been scaled by a factor of 1/100. The shaded area shows the hadronization uncertainties and the renormalization uncertainties of the NLO calculations added in quadrature. For clarity, the NC uncertainties are shown only. The CC uncertainties are of similar size.

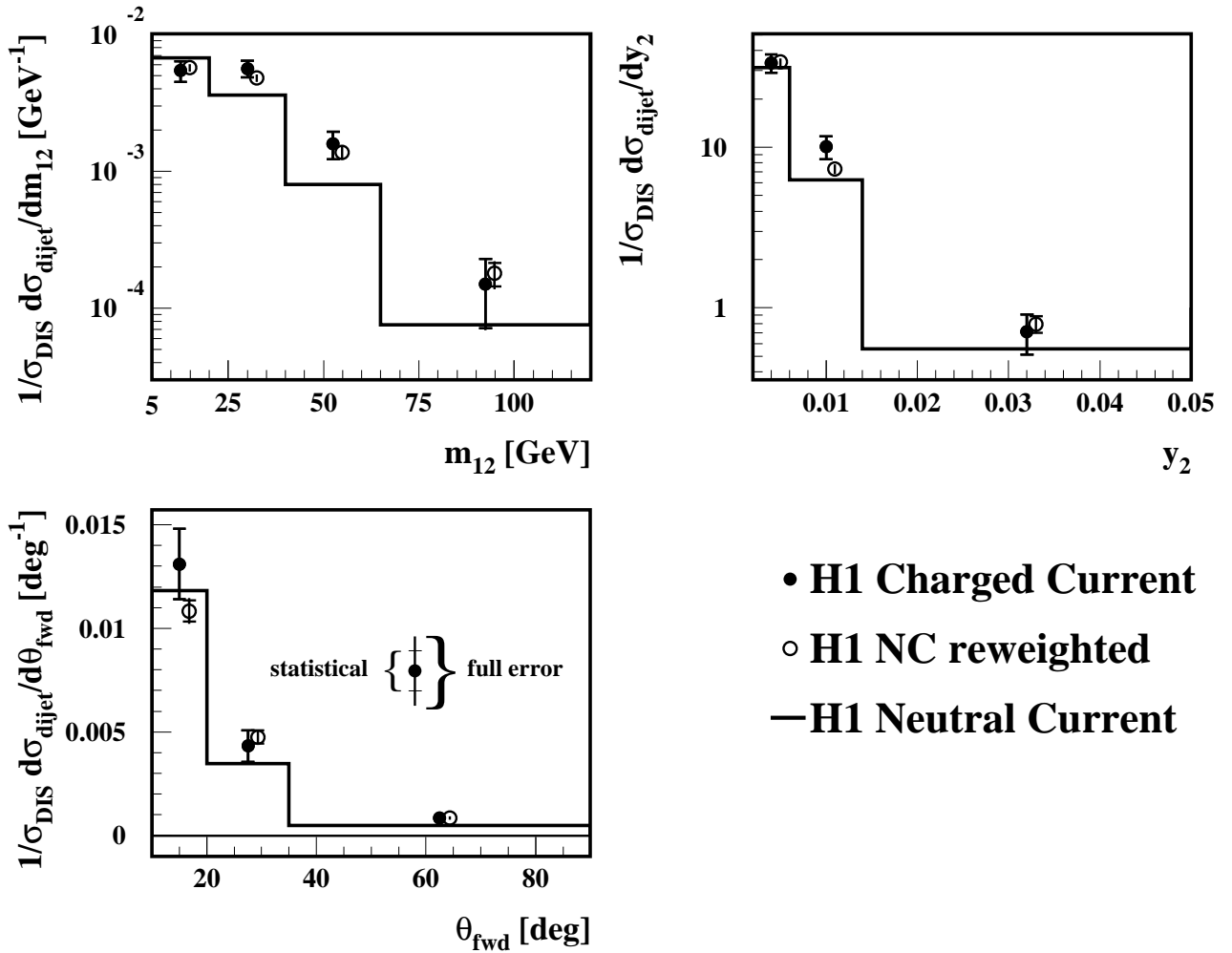


Figure 10: The distributions of m_{12} , y_2 and θ_{fwd} in CC events (full circles) and the corresponding distribution in NC events with reweighting (empty circles) as described in the text. The solid histogram corresponds to the NC distributions without reweighting, which are also shown as data points in Figures 6 and 8. The same jet selection criteria as above are applied.